Ocean Modelling 123 (2018) 86–97

Contents lists available at ScienceDirect

Ocean Modelling

journal homepage: www.elsevier.com/locate/ocemod

Impacts of wave-induced circulation in the surf zone on wave setup

Thomas Guérin, Xavier Bertin*, Thibault Coulombier, Anouk de Bakker

UMR 7266 LIENSs CNRS-Université de La Rochelle, 2 rue Olympe de Gouges, La Rochelle 17000, France

ARTICLE INFO

Keywords:
Wave setup
Numerical model
Vortex force
Undertow
Wave breaking

ABSTRACT

Wave setup corresponds to the increase in mean water level along the coast associated with the breaking of short-waves and is of key importance for coastal dynamics, as it contributes to storm surges and the generation of undertows. Although overall well explained by the divergence of the momentum flux associated with short waves in the surf zone, several studies reported substantial underestimations along the coastline. This paper investigates the impacts of the wave-induced circulation that takes place in the surf zone on wave setup, based on the analysis of 3D modelling results. A 3D phase-averaged modelling system using a vortex force formalism is applied to hindcast an unpublished field experiment, carried out at a dissipative beach under moderate to very energetic wave conditions ($H_{m0} = 6$ m at breaking and $T_p = 22$ s). When using an adaptive wave breaking parameterisation based on the beach slope, model predictions for water levels, short waves and undertows improved by about 30%, with errors reducing to 0.10 m, 0.10 m and 0.09 m/s, respectively. The analysis of model results suggests a very limited impact of the vertical circulation on wave setup at this dissipative beach. When extending this analysis to idealized simulations for different beach slopes ranging from 0.01 to 0.05, it shows that the contribution of the vertical circulation (horizontal and vertical advection and vertical viscosity terms) becomes more and more relevant as the beach slope increases. In contrast, for a given beach slope, the wave height at the breaking point has a limited impact on the relative contribution of the vertical circulation on the wave setup. For a slope of 0.05, the contribution of the terms associated with the vertical circulation accounts for up to 17% (i.e. a 20% increase) of the total setup at the shoreline, which provides a new explanation for the underestimations reported in previously published studies.

1. Introduction

Wave setup corresponds to the increase in mean water level along the coast that accompanies the breaking of short waves. Being one of the components of storm surges, wave setup is of key importance during storms and can contribute to storm-induced damage and flooding along the coast. Under energetic wave conditions, wave setup can even dominate the storm surge along coasts bordered by narrow to moderately-wide shelves (e.g. Nicolae-Lerma et al., 2017) or at volcanic Islands (Kennedy et al., 2012). Over the last decade, several studies also revealed that wave breaking over the ebb shoals of shallow inlets (Malhadas et al., 2009; Dodet et al., 2013) and large estuaries (Bertin et al., 2015; Fortunato et al., 2017; Bertin et al., 2017) drives a setup that can propagate at the scale of the whole backbarrier lagoon or estuary and contribute to the flooding of low-lying zones. Through the tilting of the free surface elevation, wave setup also causes a barotropic pressure gradient. The local imbalance between vertically varying wave forces and this pressure gradient contributes to the development of a bed return current, also referred to as undertow (Garcez-Faria et al., 2000). During storms, undertows are responsible for large offshore sand transport, thereby contributing to beach erosion (Thornton et al., 1996; Aagaard et al., 2013). For these reasons, there is a clear need to understand the physical processes that drive wave setup and to predict it accurately in numerical models.

The first experimental observations of wave setup were made by Saville (1961), on a laboratory beach of constant slope. Longuet-Higgins and Stewart (1964) then proposed a theoretical explanation for this phenomenon by introducing the concept of radiation stress, which correspond to the momentum flux associated with short-wave propagation. In the nearshore, depth-limited wave dissipation causes a gradient of radiation stress, which acts as a horizontal pressure force and tilts the water level until a balance is reached with the subsequent barotropic pressure gradient.

There is an overall agreement that the wave setup is quantitatively well predicted in the outer part of the surf zone (typically in water depths greater than a few meters), but remains underpredicted at the

* Corresponding author.
E-mail addresses: thomas.guerin@univ-lr.fr (T. Guérin), xavier.bertin@univ-lr.fr, xbertin@univ-lr.fr (X. Bertin), thibault.coulombier@univ-lr.fr (T. Coulombier), anouk.de_bakker@univ-lr.fr (A. de Bakker).

https://doi.org/10.1016/j.ocemod.2018.01.006
Received 28 July 2017; Received in revised form 26 January 2018; Accepted 28 January 2018
Available online 31 January 2018
1463-5003/

shoreline (e.g. Raubenheimer et al., 2001). The study of Apotsos et al. (2007) proposed an explanation to this underestimation, suggesting that this problem can be solved by adding both the bottom stress due to the offshore-directed mean flow, or undertow, and the wave roller in the balance equation between the cross-shore radiation stress gradient and the pressure gradient associated with the wave setup. Michallet et al. (2011) applied a 1D model that solves coupled equations representing wave roller, water level and undertow to hindcast a barred beach laboratory experiment and showed that accounting for wave skewness increased undertows and wave setup along the coast substantially.

The numerical modelling study of Bennis et al. (2014) supports the hypothesis according to which the bottom stress may impact the setup and showed that the wave-induced turbulent mixing can also increase the wave setup through an increase of the bottom shear stress.

In the present study the effect of the wave-induced circulation on the setup is further explored by using a 3D phase-averaged modelling system, with the vortex-force formalism of Ardhuin et al. (2008a). First, the modelling system is validated through a high-resolution hindcast of water levels, waves and bottom current measurements obtained at a dissipative beach under moderate to storm conditions. Second, the case of an idealized beach with a constant slope is considered in order to analyse the impact of the wave-induced circulation on the wave setup for steeper slopes.

The study area and the modelling system are described in the following sections (Sections 2 and 3). The results are presented in Section 4, followed by an extensive discussion on the model limitations, the impact of the wave breaking parameterisation, and the role of the wave-induced circulation on the setup (Section 5). Finally, the main findings are summarised in the conclusions and perspectives are also presented (Section 6).

2. Study area and field campaign

2.1. Study area

The Saint-Trojan beach is located in the central part of the French Atlantic coast (Fig. 1), along the south-west part of the Oléron Island, which corresponds to a 8 km-long sandspit, bound to the south by the Maumusson Inlet (Bertin et al., 2005). The continental shelf in front of the study area is about 150 km wide, with a very gently sloping shoreface, the isobath 20 m being found about 10 km to the west of the beach. The tidal regime in this region is semi-diurnal and macrotidal, with a tidal range varying between about 2 m during neap tides and 5.5 m during spring tides. Tidal currents remain weak at the studied beach and tidal impact is mostly restricted to water level variations. According to Bertin et al. (2008b) and Bertin et al. (2015), yearly-mean deep water wave conditions are characterized by a significant height (H_s) of 2 m, a peak period (T_p) of 10 s and a mean direction of 285°*N*. During storms, H_s can reach episodically 8–10 m in deep water, with a T_p exceeding 20 s and a westerly direction (Bertin et al., 2005; 2015). Due to the very gently sloping shoreface and the wide continental shelf, the most energetic waves suffer strong dissipation and their H_s hardly exceeds 5 m at the breaking point (Bertin et al., 2008a). This beach is mainly made of fine and well sorted sands ($d_{50} = 0.18 - 0.22$ mm), which together with the energetic wave climate and the macrotidal range cause its morphology to be non-barred and dissipative. Small-amplitude intertidal bars can only develop after the persistence of fair weather conditions. Its slope typically ranges from about 0.0015 at the shoreface to 0.015 in the intertidal area (Bertin et al., 2008b), although a berm usually develops in the course of the summer period, with a slope reaching 0.04. Due to the persistence of low to moderate-energy wave conditions in autumn 2016 and early winter 2017, such a berm was still present during our field campaign. This gently sloping morphology and the presence of a shallow shoreface induce a strong wave refraction, so that the wave angle at breaking is usually small, typically less than 10° (Bertin et al., 2008a).

2.2. Field campaign and data processing

A field campaign was carried out in early February 2017, under offshore waves characterized by H_s reaching 10 m, which corresponds to a return period on the order of one year (Nicolae-Lerma et al., 2015). Such conditions were awaited for the whole winter because they were

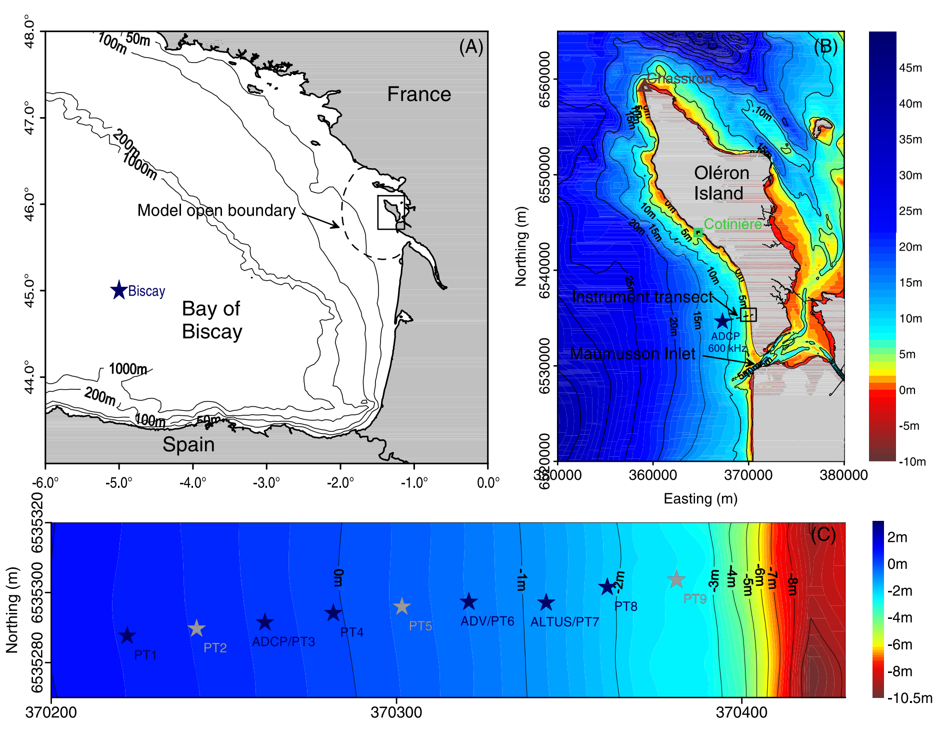

Fig. 1. (A) Location of the study area in the Bay of Biscay, with location of the Oléron Island (black box) and the Biscay buoy (blue star). (B) Bathymetric map of the study area (in m MSL), with the location of the offshore ADCP (blue star) and the instrumented cross-shore profile (dashed line). (C) Zoom on the intertidal zone with the location of the instruments used (blue star) and not used (grey star) in this study. Coordinates of (B) and (C) are in meters (Lambert-93 projection). (For interpretation of the references to color in this figure legend, the reader is referred to the web version of this article.)

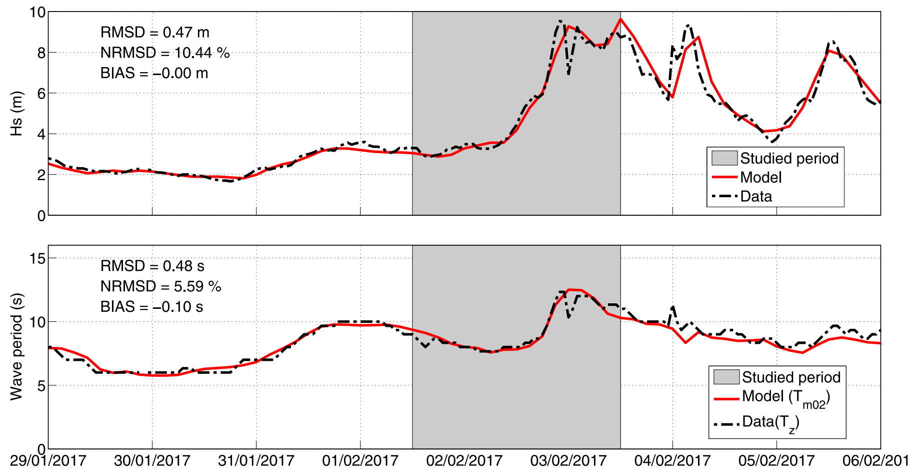

Fig. 2. Model/data comparison at the Biscay buoy:(a) H_s, and (b) $T_{m0,\ 2}$ (model) versus T_z (data ; spectral equivalent of $T_{m0,\ 2}$).

expected to drive large setup along the coast, which is the main purpose of this study. An Acoustic Doppler Current Profiler (ADCP) with a frequency of 600 kHz and equipped with a pressure sensor was deployed about 3 km offshore (Fig. 1-(B)). In the intertidal zone, 9 pressure transducers (PT) were deployed (Fig. 1-(C)) as well as a second ADCP with a head frequency of 2 MHz mounted with a pressure sensor at the location of PT3. These pressure sensores were buried between 0.05 and 0.10 m of sand, in order to avoid dynamic pressure errors. Unfortunately, only 6 PTs could be used for further analysis since the PT9 was not continuously submerged during a sufficiently long time, while the recorded signals of PT2 and PT5 presented unrealistic drifting (probably due to sand infilling below the transducer membrane) and were therefore discarded for the present study. The measurement period covered four tidal cycles, from February 1st to 3rd, characterized by a tidal range of 3.5–4 m. Deep water wave conditions measured at the Biscay buoy show that H_s increased from 2.0 m at the beginning of the campaign to 9.5 m on the 3rd of February (Fig. 2).

For each sensor, bottom pressure measurements were first corrected for sea level atmospheric pressure measured at the nearby meteorological station of Chassiron (Fig. 1-(B)). The entire record was split into consecutive bursts of 20 min and the bursts in which the sensor was alternatively dry were not considered. Bottom pressure energy density spectra $E_p(f)$ were computed using a Fast Fourier Transform, with 19 Hanning-windowed segments (38 degrees of freedom). These pressure spectra were then converted into elevation spectra $E(f)$ considering linear wave theory. The significant wave height (H_s) was computed as:

$$H_s = 4\sqrt{m_0} \tag{1}$$

with

$$m_0 = \int_{f_{min}}^{f_{max}} E(f)df \tag{2}$$

where f_{max} was set to 0.4 Hz, a value for which the pressure correction reaches about 13 by 3 m water depth, which is well below the threshold of 100 to 1000 recommended by Bishop and Donelan (1987). f_{min} is time-varying and defined following Roelvink and Stive (1989) or Hamm and Peronnard (1997) as half of the continuous peak frequency f_p, the latter being computed at the offshore ADCP as:

$$f_p = \frac{m_0^2}{m_{-2}\ m_1} \tag{3}$$

where

$$m_k = \int_{f_{min}}^{f_{max}} f^k E(f)df \tag{4}$$

The continuous peak frequency was preferred to the discrete one because it is a more stable parameter, particularly when locally-generated wind waves are superimposed to remote swells. The time-varying approach was related to the doubling of the incident peak period during the field campaign with a very high level of energy in the infragravity (hereafter IG) band, which must be separated properly from the gravity band.

In order to compute wave setup as accurately as possible, the position of each sensor was carefully measured with a differential GNSS, using a post-processing technique with a base station settled on the dune crest in front of the instrumented profile. The application of this methodology to known geodetic points revealed vertical errors ranging from 0.03 to 0.05 m. The pressure sensors having a resolution of 0.003 m and a 0.3% accuracy, a conservative error propagation results in errors on wave setup smaller than 0.06 m. Finally, the intertidal beach topography was surveyed at each low tide using the differential GNSS described above, but, surprisingly, revealed very small morphological changes, lower than 0.1 m along the cross-shore profile of the instruments.

3. The modelling system

3.1. Overview of the modelling system

The core of the modelling system used in this study is the Semi-implicit Cross-scale Hydroscience Integrated System Model (SCHISM) of Zhang et al. (2016), which is an upgrade from the model SELFE of Zhang and Baptista (2008). It is a 3D, parallelized, unstructured-grid model and presents the main feature of combining an Eulerian-Lagrangian method to treat the advection in the momentum equations with semi-implicit schemes, which relaxes the numerical stability constraints of the model. The coupling with other modules is made at the source code level, which share the same unstructured grid and domain decomposition and exchange variables directly through memory. In this study, the circulation model is coupled with an upgrade version of the third generation, spectral wind wave model (WWM) of Roland et al. (2012). It simulates gravity wave generation and propagation by solving the wave action equation (Komen et al., 1996), which reads:

$$\frac{\partial N}{\partial t} + \nabla_{\mathbf{x}}\cdot(\dot{\mathbf{x}}N) + \frac{\partial(\dot{\sigma}N)}{\partial\sigma} + \frac{\partial(\dot{\theta}N)}{\partial\theta} = S_{tot} \tag{5}$$

where σ is the relative wave frequency, θ is the wave direction, $N = E/\sigma$ is the wave action (with E being the variance density of the surface elevation), $\nabla_{\mathbf{x}}$ is the horizontal gradient operator, $\dot{\mathbf{x}}$ is the propagation velocity in space, $\dot{\sigma}$ and $\dot{\theta}$ are respectively the propagation velocities in frequency and direction, and S_{tot} is the sum of the source terms (i.e. including energy input due to wind and nonlinear wave-wave interactions, and energy dissipation due to whitecapping, depth-induced breaking, and bottom friction). WWM is coupled to SCHISM and shares the same unstructured grid and domain-decomposition.

3.2. Vortex-force formalism

In order to represent the 3D wave-induced circulation in our modelling system, the vortex-force formalism proposed by Ardhuin et al. (2008a) and based on a generalized Lagrangian mean approach (Andrews and McIntyre, 1978) has been implemented in the model following Bennis et al. (2011). Since Mellor (2003) first developed a different three-dimensional approach for explaining the wave-current coupling, some intense debate took place during the last decade (e.g. Ardhuin et al., 2008b; Mellor, 2016). However, the vortex-force theory has already been shown to be accurate in adiabatic conditions (Bennis et al. (2011), and cf. Appendix Appendix A) but also in conditions dominated by wave dissipation such as surf zones (Uchiyama et al., 2010; Kumar et al., 2012; Moghimi et al., 2013).

The vortex-force framework considers the so-called quasi-Eulerian velocity $\hat{\mathbf{u}} = (\hat{u}, \hat{v}, \hat{w})$, which equals the mean Lagrangian velocity $\mathbf{u} = (u, v, w)$ minus the Stokes velocity $\mathbf{u_s} = (u_s, v_s, w_s)$, and satisfies the continuity equation:

$$\nabla \cdot \hat{\mathbf{u}} = 0 \tag{6}$$

with $\nabla = \left(\frac{\partial}{\partial x}, \frac{\partial}{\partial y}, \frac{\partial}{\partial z}\right)$.

As for the momentum equation, resolved at each sigma-level, it reads:

$$\frac{D\hat{u}}{Dt} = f\hat{v} - \frac{1}{\rho}\frac{\partial p^H}{\partial x} + \frac{\partial}{\partial z}\left(\nu\frac{\partial \hat{u}}{\partial z}\right) + F_{wave,x} \tag{7}$$

along the x-axis, and

$$\frac{D\hat{v}}{Dt} = -f\hat{u} - \frac{1}{\rho}\frac{\partial p^H}{\partial y} + \frac{\partial}{\partial z}\left(\nu\frac{\partial \hat{v}}{\partial z}\right) + F_{wave,y} \tag{8}$$

along the y-axis. f is the Coriolis parameter, ρ is the water density, p^H is the hydrostatic pressure, and ν is the vertical eddy viscosity. Following Bennis et al. (2011), the two components of the wave force term read:

$$F_{wave,x} = v_s\left[f + \left(\frac{\partial \hat{v}}{\partial x} - \frac{\partial \hat{u}}{\partial y}\right)\right] - w_s\frac{\partial \hat{u}}{\partial z} - \frac{\partial J}{\partial x} + \hat{F}_{d,x} + \hat{F}_{r,x} \tag{9}$$

and

$$F_{wave,y} = -u_s\left[f + \left(\frac{\partial \hat{v}}{\partial x} - \frac{\partial \hat{u}}{\partial y}\right)\right] - w_s\frac{\partial \hat{v}}{\partial z} - \frac{\partial J}{\partial y} + \hat{F}_{d,y} + \hat{F}_{r,y} \tag{10}$$

where J is the wave-induced mean pressure, and $\hat{\boldsymbol{F}}_d$ and $\hat{\boldsymbol{F}}_r$ are the sources of quasi-Eulerian momentum due to depth-induced wave breaking and wave surface roller respectively. The latter terms are described in more detail in the following subsections.

3.3. Depth-induced wave breaking

The energy dissipation due to depth-limited wave breaking is computed according to the model of Thornton and Guza (1983) adapted to the wave action equation as described in the SWAN spectral wave model (The SWAN team, 2014), which gives the following expression for the energy dissipation D_{tot} (in $m^2.\ s^{-1}$) :

$$D_{tot} = -\frac{3B^3\overline{\sigma}}{32\sqrt{\pi}h}\, Q_b\, H_{rms}^3 \tag{11}$$

where $h = d + \eta$ is the total water depth with d and η being the bathymetry and the mean surface elevation (in m MSL) respectively, $\overline{\sigma}$ is the mean wave frequency, $Q_b = \left(\frac{H_{rms}}{\gamma h}\right)^4$ represents the fraction of broken waves where γ is a breaker index that corresponds to the maximum H_{rms} to water depth ratio in the inner surf zone. As explained by Apotsos et al. (2008) the parameters γ and B are interdependent in this wave transformation model, and the corresponding best-fit values on the wave height and energy dissipation profiles will vary from one field site to another. Several studies also showed that considering a constant γ in the surf zone is often a too simplistic assumption since it tends to increase with the bed slope $\tan\beta$ (e.g. Sallenger and Holman, 1985; Raubenheimer et al., 1996; Salmon et al., 2015). Based on our experimental data located in the inner surf zone, we computed H_{rms}/h and observed that it increases with the beach slope, from about 0.32 at the offshore ADCP location (i.e. where $\tan\beta \simeq 0.001$) until about 0.53 at the shoreline (i.e. where $\tan\beta \simeq 0.04$). At the same time it has been shown that the wave dissipation rate (represented by B) is higher on steep slopes than on mild slopes (Cacina, 1989). These two parameters were therefore computed in the model as a linear function of the bed slope (as in Sallenger and Holman (1985)):

$$\gamma = a_\gamma \tan\beta_w + b_\gamma;\ \ B = a_B \tan\beta_w + b_B \tag{12}$$

where $\tan\beta_w$ is the bed slope along the peak wave direction propagation, computed at each grid node with the neighboring elements using shape functions and $\{a_\gamma,\ b_\gamma,\ a_B,\ b_B\}$ are calibrated to give the best-fit wave height and energy dissipation profiles (i.e. when comparing with measurements of H_s and bottom current). Note that our model γ was adjusted based on the observed H_{rms} to water depth ratio in the inner surf zone and assuming that all waves had broken, although this hypothesis might be more questionable for steep beaches.

Extending this dissipation model to a spectral model (following the same approach of Eldeberky and Battjes (1996)), the energy dissipation corresponding to one energy bin reads :

$$D(\sigma,\theta) = \frac{D_{tot}}{E_{tot}}E(\sigma,\theta) = -\frac{3B^3\overline{\sigma}}{4\sqrt{\pi}h}\, Q_b\, H_{rms}\, E(\sigma,\theta) \tag{13}$$

where $E_{tot} = H_{rms}^2/8$ and $E(\sigma,\ \theta)$ are the total and discrete variance density of the surface elevation, respectively. The source of quasi-Eulerian momentum due to depth-induced wave breaking (in $m.\ s^{-2}$), also called breaking acceleration, is then computed at each vertical level as :

$$(\hat{F}_{d,x}(z), \hat{F}_{d,y}(z)) = -gf(z)\int_0^{2\pi}\int_0^{\infty}(\cos\theta, \sin\theta)\frac{k(\sigma)}{\sigma^2}D(\sigma,\theta)d\sigma d\theta \tag{14}$$

which can be expressed using the wave action $N(\sigma,\ \theta)$ as:

$$(\hat{F}_{d,x}(z), \hat{F}_{d,y}(z)) = -gf(z)\int_0^{2\pi}\int_0^{\infty}(\cos\theta, \sin\theta)\frac{k(\sigma)}{\sigma}\frac{D_{tot}}{E_{tot}}N(\sigma,\theta)d\sigma d\theta \tag{15}$$

and where $k(\sigma)$ is the wavenumber, and $f(z)$ is an empirical vertical distribution function quantifying the vertical penetration of momentum related to wave breaking, computed following Uchiyama et al. (2010) as:

$$f(z) = \frac{\cosh(k_b(z+d))}{\int_{-d}^{\eta}\cosh(k_b(z+d))dz} \tag{16}$$

where $k_b = (0.2H_{rms})^{-1}$ is a decay parameter controlling the penetration depth.

3.4. Wave roller

The source of momentum due the wave roller ($\hat{\boldsymbol{F}}_r$) is computed following the approach of Saied and Tsanis (2008) which is based on Dally and Osiecki (1995):

$$\hat{F}_{r,x}(z) = -\rho^{-1}f(z)\left(\frac{\partial R_{xx}}{\partial x} + \frac{\partial R_{xy}}{\partial y}\right) \tag{17}$$

$$\hat{F}_{r,y}(z) = -\rho^{-1}f(z)\left(\frac{\partial R_{yy}}{\partial y} + \frac{\partial R_{yx}}{\partial x}\right) \tag{18}$$

with

$$R_{xx} = 2E_r\cos^2(\theta_p);\ R_{yy} = 2E_r\sin^2(\theta_p);\ R_{xy} = R_{yx} = E_r\sin(2\theta_p) \quad (19)$$

where θ_p is the peak wave direction. The computation of the roller energy (E_r) is based on the work of Svendsen (1984):

$$E_r = \frac{1}{2}\rho c_p\frac{0.9H_{rms}^2}{T_p} \quad (20)$$

where c_p is the peak phase velocity and T_p is the peak period.

3.5. Wave-enhanced turbulence

The inclusion of the vertical mixing due to wave breaking is implemented in our turbulence closure scheme (based on Umlauf and Burchard (2003)) following the method of Moghimi et al. (2013) through the sea surface boundary condition:

$$K(z = \eta) = \frac{1}{2}B_1^{3/2}\left(\frac{|\tau_w|}{\rho} + \beta^s\ |\boldsymbol{S}^d|\right) \quad (21)$$

where K is the turbulent kinetic energy, B_1 is a constant, $\tau_w = (\tau_{w,x}, \tau_{w,y})$ is the wind stress (in kg.m^{-1}. s^{-2}), $\boldsymbol{S}^d = (S_x^d, S_y^d) = -f(z)^{-1}(\widehat{F}_{d,x}(z), \widehat{F}_{d,y}(z))$ is the source of momentum due to wave breaking integrated over the water column (i.e. in $m^2.\ s^{-2}$) and can be seen here as a (density-normalized) stress related to breaking. β^s is a coefficient that relates the amount of the energy dissipated by wave breaking that is transformed into turbulent kinetic energy and is set to 0.15 according to the study of Feddersen (2012). The length scale of the surface-injected turbulence, or surface roughness z_0^s, is eventually set to $0.6H_s$ as proposed by Terray et al. (1996) and also used by Bennis et al. (2014) and Moghimi et al. (2016), and imposed as a surface boundary condition for the turbulent mixing length l:

$$l\ (z = \eta) = \kappa z_0^s \quad (22)$$

where κ is the von Karman's constant.

3.6. Bottom friction

The model of Grant and Madsen (1979) is used to handle the bottom friction in the model under combined wave and current. This approach provides an apparent roughness length z_0^b which is a function of the grain roughness set to $1.67E - 5\ (d_{50}/12)$, the current and wave orbital velocities, and the angle between both. Similarly to the surface roughness length, this wave-current apparent bottom roughness is then injected into the turbulence closure model through the bottom boundary condition for the turbulent mixing length:

$$l\ (z = -d) = \kappa z_0^b \quad (23)$$

3.7. Model implementation

The unstructured computational grid used for the Saint-Trojan beach case is characterized by a spatial resolution ranging from 4.5 km at the offshore boundary (see Fig. 1-(B) for its extension) down to 20 m in the surf zone. 11 sigma levels are used for the vertical discretisation, and the time step is set to 10 s for both the hydrodynamic and the wave module. The tidal forcing is computed by considering the 16 main tidal constituents linearly interpolated from the regional tidal model of Bertin et al. (2012). Wind and pressure sea-level fields originate from the Climate Forecast System Reanalysis (CFSR) for the atmospheric forcing (1 h time resolution and spatial resolutions of 0.2° and 0.5° for the wind and the atmospheric pressure, respectively). The wave forcing is obtained from a regional application of the WaveWatchIII spectral wave model, configured as described in Bertin et al. (2013) and forced with the CFSR wind fields described above. Finally, the spectral space is discretized according to 30 directions and 30 frequencies ranging from 0.036 to 0.4 Hz.

4. Model validation

4.1. Introduction

Model/data comparisons were done by computing the averaged measured value for each burst (i.e. 20 min average) and comparing it to the corresponding time-averaged modelled value. For wave heights, the model spectra were integrated over the same frequency range as the data. Due to the presence of very large IG waves, the hydrodynamics was dominated by periods of about 100 s, so that velocity profiles averaged over 2 min were aliased. Alternatively, the undertows considered in this section correspond to 20 min average during the wave cycle of the ADCP, where currents were measured within a cell of 0.5 m, starting 0.2 m above the bed. Mean bias, root-mean-square discrepancy (RMSD), and Normalized RMSD (NRMSD) were then computed for every parameter. This last parameter corresponds to the RMSD normalized by the mean value of the observations. Considering the spatial resolution of our grid as well as the presence of low frequency fluctuations in observed water levels, we only considered samples where the mean water depth was higher than 0.3 m.

4.2. Water levels and short waves

The first comparison between observed and simulated wave conditions is done at the deep water Biscay buoy (Fig. 2), which is located approximately at $5.\ 00°W - 45.\ 23°N$ and in 4500 m water depth. As this buoy is located outside the computational domain of the local grid, this comparison is made with our regional WWIII model and aims to validate the wave forcing that we employed to force the local model. Very energetic conditions are reached near the end of the studied period, with H_s reaching 9.5 m. Deepwater wave conditions were very well reproduced by the model during the field experiment, with NRMSD of 10% for H_s and 6% for the mean wave period (Fig. 2).

At the shoreface, wave conditions were moderate during the first two tidal cycles with H_{m0} and T_p on the order of 2 m and 13 s at the offshore ADCP, respectively. Wave energy increased substantially during the two following tidal cycles, where H_{m0} reached 6 m and T_p reached 21 s.

At the offshore ADCP location (Fig. 3), water levels and wave conditions are fairly well reproduced by the model, except during the last tidal cycle where the T_p and $T_{m0,\ 2}$ remain underestimated by 1 to 2 s. Nevertheless, a normalized root-mean-square error inferior to 11% is obtained for all parameters (when for the water level we compute NRMSD as the RMSD divided by the mean tidal range), which corresponds to the state-of-the-art considering recently published studies using phase-averaged approaches (e.g. Olabarrieta et al., 2011; Bruneau et al., 2011; Delpey et al., 2014). At the intertidal stations, the simulated water level is globally very well reproduced during the two-day period but it remains underestimated at the end of the last one (Fig. 4), the latter bias being mainly due to the underestimated wind surge (probably because of the atmospheric forcing, which is not accurate-enough). In all stations, both field measurements and model results show that the short waves were depth-limited and, therefore, tidally modulated (Fig. 5). In more details, the wave height always increases as and when the water depth increases, which suggests that the sensors were always located inside the surf zone. Good predictions are obtained for the wave heights (Fig. 5), although H_s is only constrained by the water depth and the γ parameter, which was adjusted based on field measurements (see Section 3.3).

4.3. Undertow

Consistent comparisons between measured and simulated currents were only feasible at the surf zone ADCP location and for the first

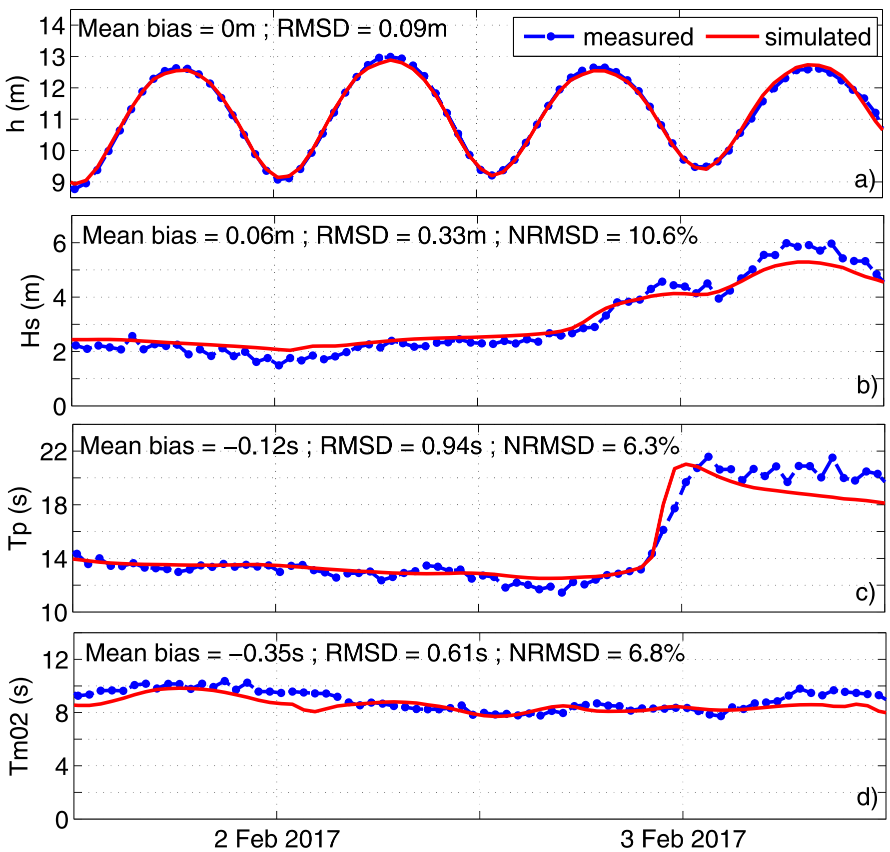

Fig. 3. Measured and simulated water level, H_s, T_p, and $T_{m0,2}$ at the offshore ADCP location.

measurement cell along the vertical (starting from the bottom), since the bursts for the other cells were not temporally long-enough to low-pass filter the effect of IG waves, which cause the cross-shore velocity to be alternatively onshore and offshore directed. Fig. 6 shows the comparison between the measured cross-shore velocity, which was computed by time-averaging the cross-shore velocity signal for each 20 min burst, and the simulated quasi-Eulerian velocity at $z = 0.47$ m from the bed (i.e. the center of the measurement cell). The measured bottom velocity is almost always negative indicating the presence of an undertow (the positive values correspond mainly to times where the measurement cell is not limited to the lower part of the water column due to relatively low water levels), and one can note that it only reaches about $-0.3\,\mathrm{m.s^{-1}}$ even under very energetic conditions, very probably because the location of the instrument remains close to the shoreline in comparison to the large surf zone width. This hypothesis is supported by model results, which suggest that undertows up to $-0.7\,\mathrm{m.s^{-1}}$ developed 500 to 1000 m from the shoreline. An overall good agreement is obtained between measured and simulated bottom cross-shore velocity, though an unexplained bias is observed during the third tidal cycle.

4.4. Setup

Comparisons between the total surge computed from measurements and from the model at the different intertidal stations are shown in Fig. 7, where it can be seen that a good overall agreement is obtained between both. It is important to note that the atmospheric surge only reached a maximum of about 10 cm during almost the full measurement period, meaning that the essential part of the total surge is due to the setup, except during the last 1.5 h which has been removed for the present comparison because of partly inaccurate atmospheric forcing for this particular time. In more details, the joint analysis of Fig. 4 and 7 reveals that the accuracy of setup predictions does not deteriorate in shallow water, with a nil to very small negative bias at PT7 and PT8, where the water depth is lower than 1.0 m.

5. Discussion

5.1. Model predictive skills and limitations

In this study, an existing 3D phase-averaged modelling system was improved to adequately represent the main effects of short waves on the hydrodynamic circulation in the nearshore, namely: the wave breaking and roller accelerations, the enhanced bottom stress and vertical mixing. This modelling system was applied to hindcast a field experiment carried out at a dissipative beach under moderate-energy to extreme wave conditions, with offshore H_{m0} exceeding 9.0 m and H_{m0} at breaking reaching 6.0 m. Model/data comparison for wave parameters, water levels and undertows showed predictive skills within the state-of-the-art (Moghimi et al., 2013; Kumar et al., 2012), which should be highlighted because high-resolution hindcasts of surf zones under this range of wave heights is very scarce in the literature. The comparison between observed and modelled total surge showed that the improved modelling system was able to reproduce the surge with a NRMSD of the order of 20%, and with a negative mean bias of about 5 cm, which remains in the error margin of the measurements. While model/data comparisons of wave setup under storm conditions are very limited in the literature, probably owing to the inherent difficulty to collect measurements under such conditions, the results obtained in this study are of similar accuracy compared to wave setup predictions obtained for low to moderate wave conditions and with a 1D analytical model (e.g. Apotsos et al., 2007), or under high energetic conditions but with a 3D phase-resolving wave model (e.g. Nicolae-Lerma et al., 2017).

In order to analyse the impact of the different wave-induced effects on the results (except for the wave breaking parameterisation which will be discussed in the next section), some sensitivity tests were carried out. It first appears that, β^s, which relates the amount of the energy dissipated by wave breaking that is transformed into turbulent kinetic

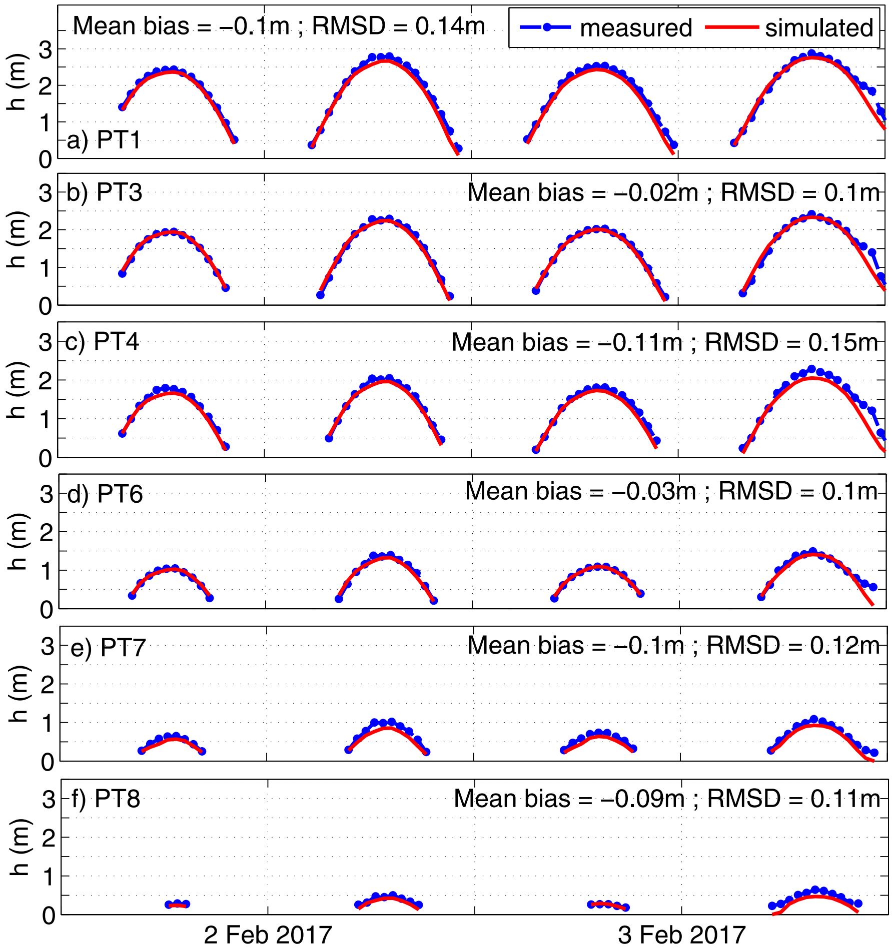

Fig. 4. Measured and simulated water level at the intertidal stations.

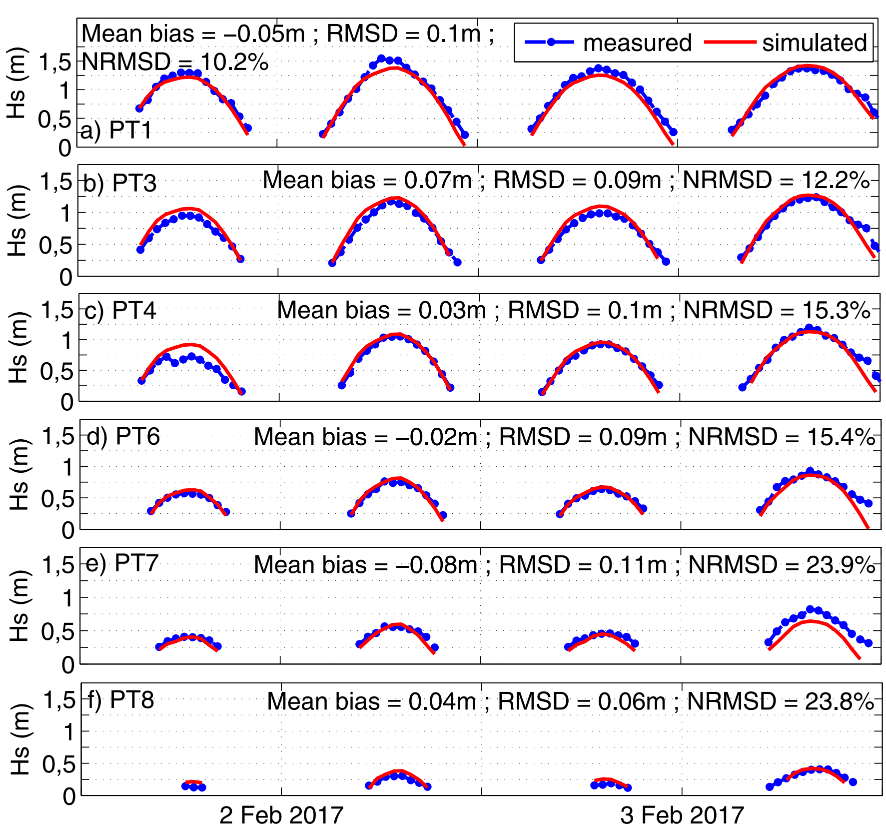

Fig. 5. Measured and simulated H_s at the intertidal stations.

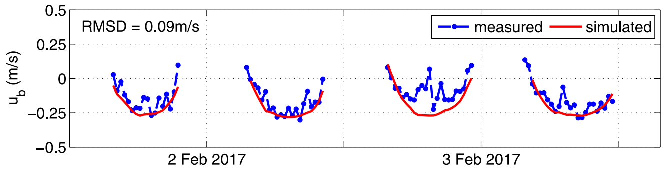

Fig. 6. Measured cross-shore current versus simulated quasi-Eulerian cross-shore velocity at the surf zone ADCP location (PT3 station), and at z = 0.47 m from the bed.

energy, did not impact the results substantially when varying it from 15% (i.e. the best-fit value corresponding to the study of Feddersen, 2012) to 100%, probably due to the relative weakness of the wave-induced circulation that is present even without wave-induced turbulence. Similarly, the consideration in the turbulence closure model of an increased bottom mixing length due to the presence of waves did not reveal much impact on the water levels results. While the inclusion of the roller effect slightly increased the wave setup predictions, which corroborates the findings of Apotsos et al. (2007), this effect remained weak, probably due to the unbarred morphology of the Saint-Trojan Beach. However, we employed a simplified approach to represent roller effects, which might be questionable for barred beaches, where the roller would have a larger contribution. Further research is needed, for instance regarding the parameterisation of the roller area as a function of the breaking regime.

Another process that might influence the observed setup is the presence of very large IG waves during the measurement period, with $H_{m0,\ IG}$ exceeding 1.8 m in the nearshore during the last tidal cycle. While the analysis of these IG waves is outside the scope of this paper and deserves a specific study, one can wonder what would be the impact of not representing this phenomenon in our modelling system. Firstly, across the surf zone, a substantial amount of energy is transferred from the gravity to the IG band through non-linear interactions. In the present modelling system, short wave energy loss across the surf zone is represented mainly through depth-limited breaking, which is then injected in the momentum equations of the circulation model. It is therefore possible that the amount of energy that is injected in the momentum equations is overestimated. Secondly, the measured current velocities associated with the most energetic IG waves were seen to be asymmetric and to reach about 2 m.s^{-1} in the very nearshore, which can potentially cause a non-zero resulting bottom stress over an IG wave period and thus impact the wave setup.

5.2. Importance of wave breaking parameterisation

The studied beach has already been the subject of several modelling studies, which aimed at computing the annual longshore transport (Bertin et al., 2008b) and validating a modelling system (Bertin et al., 2009). In these studies the beach displayed a very flat morphology with a constant slope on the order of 0.015, and significant wave heights were well reproduced (NRMSD of the order of 15%) using a constant γ parameter in the wave breaking model and set to 0.39 (equivalent to 0.55 based on H_s in Bertin et al., 2009). When applied to the present dataset, this parameterisation only allowed obtaining fair wave height predictions in the beach lower part (Fig. 8-a)). In the beach upper part, where the bottom slope increases by a factor of 2 to 3, wave heights were underestimated by a factor of two. This problem led us to implement an adaptive breaking parameterisation, which improved our wave-height predictions from the gently sloping lower beach to the steep upper beach (Fig. 8-b)), as shown by the decrease of the RMSD from 0.13 m to 0.09 m. As the wave setup is controlled mainly by wave dissipation, the surge predictions are also substantially improved with the adaptive breaking parameterisation (Fig. 9). The NRMSD for the whole dataset decreases from 31% to 22% while the bias is reduced by a factor of 2 when switching from constant to variable breaking parameterisation, while the main improvements are found where the beach slope exceeds 0.03. As shown by for instance Barthelemy (2017), these results suggest that an adaptive wave breaking parameterisation is particularly relevant in coastal environments where the bottom slope varies strongly, such as barred beaches or tidal inlets.

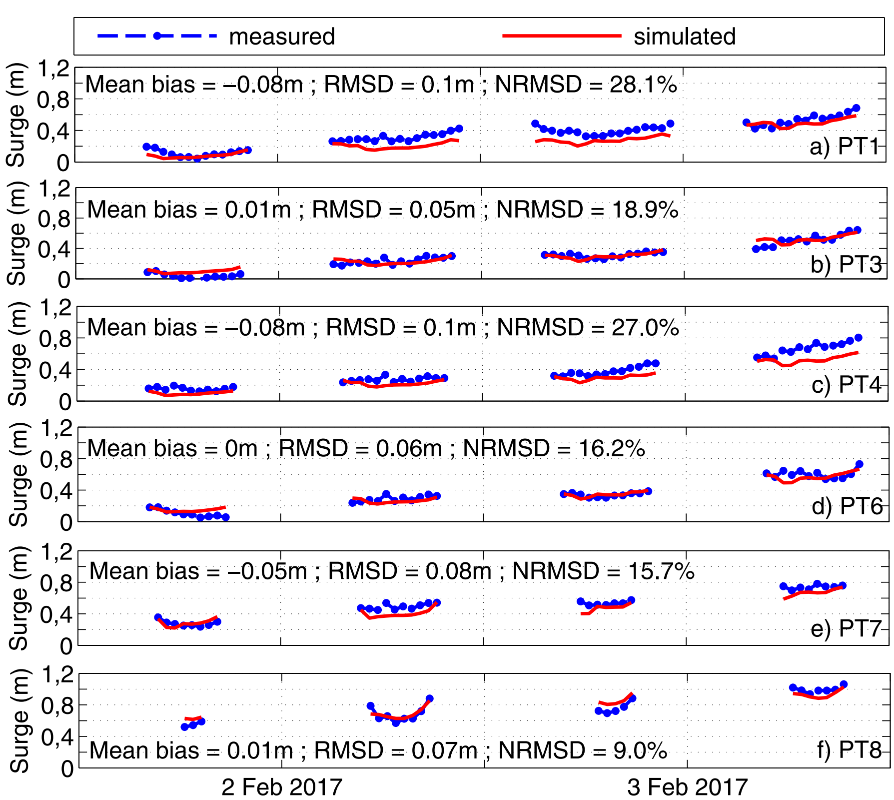

Fig. 7. Measured and simulated total surge at the intertidal stations.

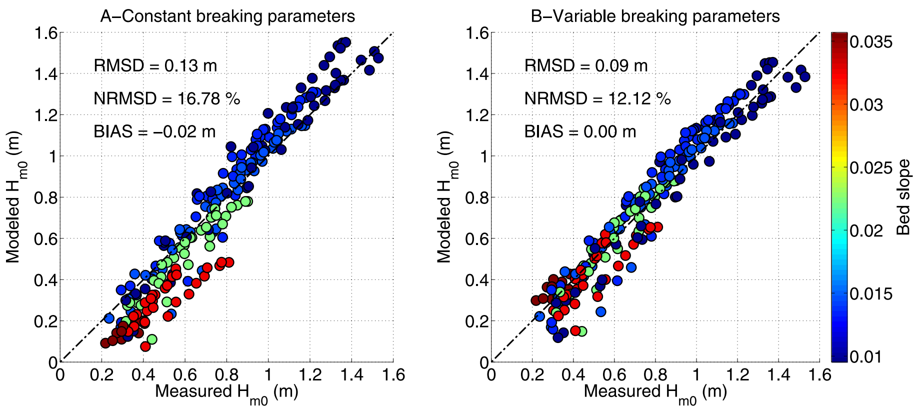

Fig. 8. Simulated against observed H_{m0} for (a) constant wave breaking parameters and (b) adaptive wave breaking parameters.

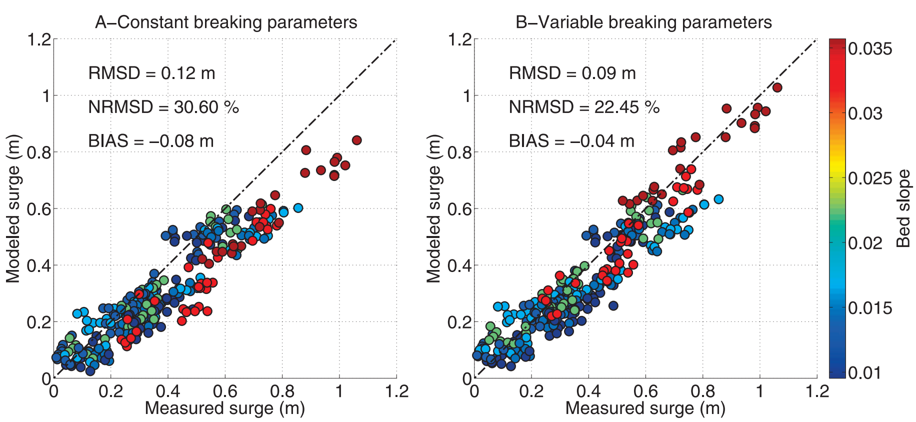

Fig. 9. Simulated against observed total surge for (a) constant wave breaking parameters and (b) adaptive wave breaking parameters.

5.3. Impact of the beach slope on the wave setup

As proposed in the study of Apotsos et al. (2007), the wave setup can be increased by representing a bottom stress term associated with the undertow into the classical 1D cross-shore balance equation between the wave momentum flux gradient (i.e. the radiation stress gradient when following Longuet-Higgins and Stewart, 1964) and the barotropic pressure gradient associated with the setup. A first test to verify this hypothesis in Saint-Trojan is to simply compare 3D and 2DH runs since the depth-varying wave-induced circulation is not represented when using a 2DH configuration. The comparison between the surge simulated with these two configurations can be seen on the scatter plot of Fig. 10, which reveals only very marginal improvements with the 3D approach compared to the 2DH approach. This behaviour could appear to be in disagreement with the conclusions of Apotsos et al. (2007) or suggest that other parameters differ between both studies.

Interestingly, the surf zone-integrated beach slope of the two field sites studied by Apotsos et al. (2007) (i.e. beaches near Duck in North Carolina and near Egmond in The Netherlands) is substantially higher than the one of our field site, which ranges from 0.003 at low tide during the storm peak to 0.015 during the first high tide. We thus applied the model to the case of an idealized beach with different constant slopes in order to analyse the extent to which the vertical circulation can affect the difference between 2DH- and 3D-simulated wave setup. For this idealized case, we used a computational grid 1.85 km -long and 1.5 km wide, a grid resolution ranging from 15 m along the open boundary to 2 m along the coast, a time step of 5 s, and 41 sigma levels. Constant, normally-incident waves were considered with $T_p = 12$ s and H_{m0} at breaking (hereafter H_b) of 1.0, 3.0 and 5.0 m, without tidal nor atmospheric forcing. The roller acceleration was turned off for these idealized test cases in order to focus only on the contribution of the

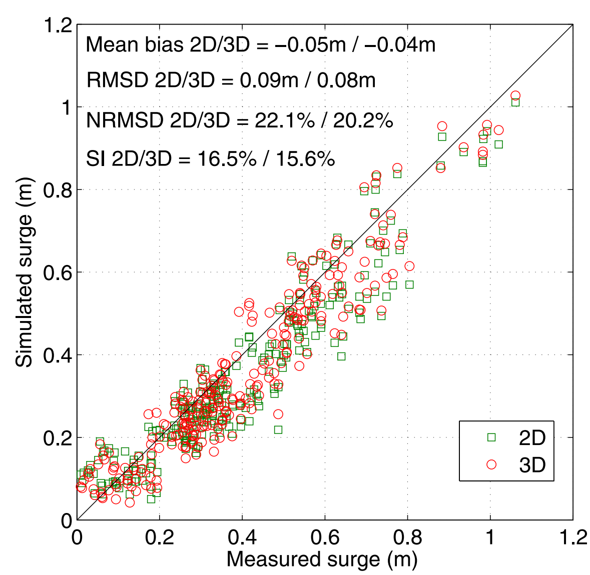

Fig. 10. Scatter plot of measured versus simulated total surge.

wave-induced circulation on the setup. Since no specific wave breaking parameterisation is adequate for all considered beach slope, the approach of Apotsos et al. (2008) is used here by holding B constant to 1 and considering their highest mean best-fit value for γ which equals 0.51 for the Thornton and Guza (1983) model. The corresponding momentum equation along the cross-shore axis satisfies:

$$\frac{D\hat{u}}{Dt} = -\frac{1}{\rho}\frac{\partial p^H}{\partial x} + \frac{\partial}{\partial z}\left(\nu\frac{\partial \hat{u}}{\partial z}\right) + F_{wave,x} \tag{24}$$

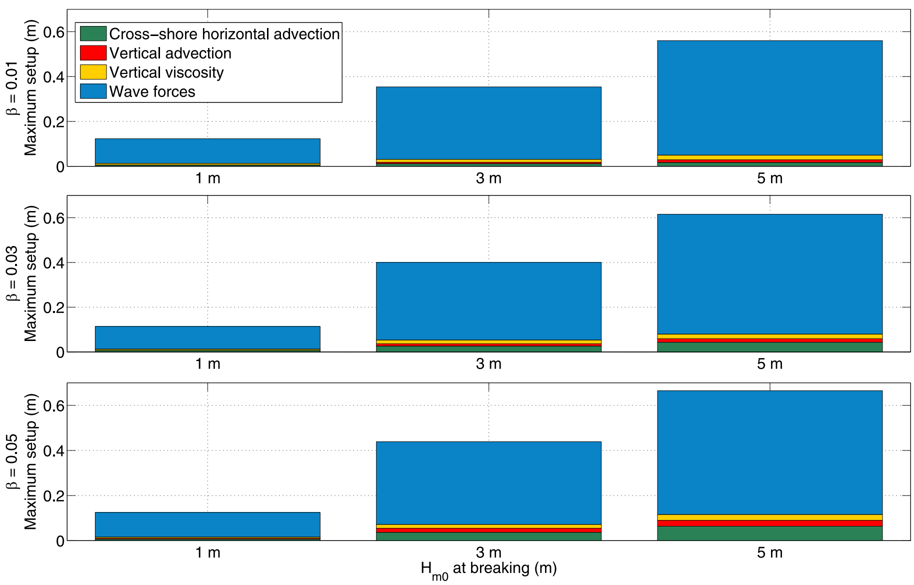

Fig. 11. Contribution of each term of Eq. (25) to the wave setup, for an idealized beaches with constant slopes of 0.01, 0.03 and 0.05 and wave height at breaking of 1, 3 and 5 m.

which, once the steady state is reached and depth-integrated, is equivalent to:

$$g\frac{\partial\eta}{\partial x} = \frac{1}{h}\int_{-d}^{\eta}\left(-\hat{u}\frac{\partial\hat{u}}{\partial x} - \hat{v}\frac{\partial\hat{u}}{\partial y} - \hat{w}\frac{\partial\hat{u}}{\partial z} + \frac{\partial}{\partial z}\left(\nu\frac{\partial\hat{u}}{\partial z}\right) + F_{wave,x}\right)dz \tag{25}$$

Aiming to analyse the contribution of each term of the right-hand side (RHS) of Eq. (25) to its left-hand side (which gives the wave setup), we use the model outputs (i.e. quasi-Eulerian velocity, vertical viscosity, and wave force outputs) to compute the partial change in mean elevation (or setup contribution) associated with each RHS term. The total wave setup can thus be written:

$$\eta = \eta_{\hat{u}} + \eta_{\hat{v}} + \eta_{\hat{w}} + \eta_{\nu} + \eta_{wafo} \tag{26}$$

where $\eta_{\hat{u}}$, $\eta_{\hat{v}}$, $\eta_{\hat{w}}$, $\eta_{\hat{v}}$ and η_{wafo} are the setup contributions associated with the cross-shore advection, the longshore advection, the vertical advection, the vertical viscosity and the wave force terms, respectively. Each term is computed in a similar manner, as for instance:

$$\eta_{\hat{u}}(x) = \frac{1}{gh}\int_{0}^{x}\int_{-d}^{\eta}\left(-\hat{u}\frac{\partial\hat{u}}{\partial x}\right)dzdx \tag{27}$$

for the setup contribution due to the cross-shore advection.

The results of these 9 simulations are synthesized on Fig. 11 which reveals firstly that, for a given wave height at breaking (hereafter H_b), maximum wave setup along the coast increases with the beach slope. The contribution of wave forces varies very little with the beach slope or H_b and induces a maximum setup on the order of 10–12% of H_b. However, one should note that this behaviour might be related to the constant breaking parameterisation used in these idealized tests. In contrast to the wave force, the contribution of the vertical circulation to the maximum setup increases with the beach slope, from about 10% for $\beta = 0.01$ to about 17% for $\beta = 0.05$. In more details, among the terms associated with the wave-induced circulation, the vertical viscosity term appears more relevant for a gently sloping beach while the (cross-shore) horizontal advection term becomes dominant for more sloping beaches. Interestingly, for a given beach slope, the respective contribution of each term varies very little with H_b.

In order to illustrate how these different mechanisms vary spatially, we computed each term along a cross-shore profile located at mid-grid width for the steepest considered beach slope ($\beta = 0.05$) with $H_b = 5m$ (Fig. 12). In this figure, the sum of the contribution of the different terms is called η_{RHS} and is also plotted in order to verify that it approximately equals the simulated wave setup η (the remaining disparity between the two being due to the post-processing of model results, which doesn't match exactly the model algorithm). Moreover, one can note that the longshore advection term $\eta_{\hat{v}}$ is zero, as it can be expected for shore-normal waves.

While the wave setup simulated using a 2DH configuration is only due to the wave force term (i.e. $\eta = \eta_{wafo}$), it can be clearly seen on Fig. 12 that this is not the case when using a 3D configuration. The contribution of the advection terms ($\eta_{\hat{u}}$ and $\eta_{\hat{w}}$) and the vertical viscosity term (η_{ν}) become positive 50–80 m from the shoreline, which causes an increase of the wave setup compared to the case where only the wave force term is taken into account (i.e. in a 2DH configuration). These results could explain the underestimated setup along the shoreline found in Raubenheimer et al. (2001) and Apotsos et al. (2007). It is also interesting to note that the advection terms contribute slightly to increase the set-down compared to the simulation where only the wave force term is considered.

6. Conclusions

A yet unpublished dataset of water levels, wave parameters and bottom currents was obtained at the dissipative beach of Saint-Trojan (France) during early February 2017 under storm conditions, with offshore H_{m0} exceeding 9.0 m and H_{m0} at breaking reaching 6.0 m. An existing 3D phase-averaged modelling system was improved to adequately represent the main effects of short waves on the hydrodynamic circulation and revealed good predictive skills and stability, even for a range of wave heights for which high-resolution model applications are very scarce. The comparison between a constant and an adaptive wave breaking parameterisation revealed that wave height and setup predictions in the surf zone are substantially improved with the second approach, which suggests that adaptive parameterisations should be relevant for coastal zones with varying bottom slopes, such as barred beaches and tidal inlets. The comparison between a 2DH and a 3D run revealed only very marginal improvements with the second approach, which suggests that the impact of the vertical circulation on wave setup is very weak at the studied dissipative beach. However, the application of the model at idealized beaches with varying slopes and wave heights revealed that the relative contribution of the horizontal and vertical advection terms and the vertical viscosity term to the total setup increase with the beach slope, reaching about 17% (i.e. a 20% increase) for $\beta = 0.05$. Moreover, this analysis suggests that the respective contribution of each term varies little with the wave height at breaking.

Previously published studies relying on 1D models (Raubenheimer et al., 1996; Apotsos et al., 2007) reported substantial underestimations

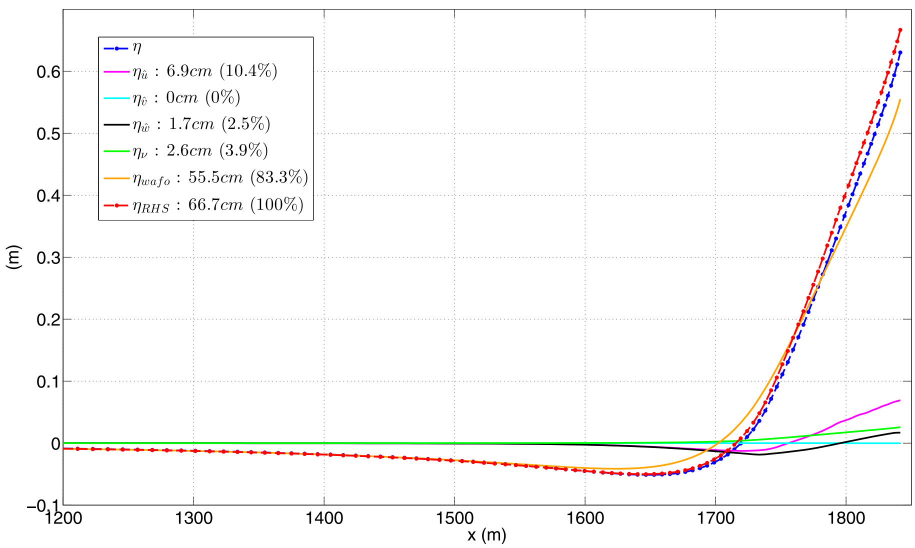

Fig. 12. Contribution of each term of Eq. (25) to the wave setup, for an idealized beach with a constant slope of 0.05 and a wave height at breaking of 5.0 m. The left-hand limit for the x-axis (i.e. $x = 1200$ m) corresponds to a water depth of 32 m.

of wave setup in shallow water. The mechanisms presented in this study provide new explanations for this problem, but will have to be verified through new field experiments at steep beaches.

Acknowledgements

This work was initiated in the scope of the research project DYNAMO, funded by the French National Research Agency (Grant agreement ANR-12-JS02-00008-01) and pursued in the scope of the Chaire Regional Program EVEX, funded by the Poitou-Charentes Region (France). AdB was partly funded by the program Prestige of Campus France (grant agreement n° PCOFUND-GA-2013-609102). We warmly thank Bastien Millescamps for the post-processing of the GPS data. Joseph Zhang, Aron Roland, and Antoine Dumon are also greatly acknowledged for their contribution to the development of the model. Baptiste Mengual explored the first ideas of this study during his M.Sc internship at LIENSs. Finally, Kevin Martins provided valuable comments about the parameterisation of wave dissipation and roller contribution.

Appendix A. Adiabatic case

The adiabatic test case presented in Bennis et al. (2011) was considered as a first test to validate the implementation of the vortex-force formalism in our modelling system. This test case consists of steady monochromatic waves shoaling and deshoaling over a bump, without wave breaking and for an inviscid fluid. Using an incident wave height $H = 1.02$ m and a wave period $T = 5.24$ s, the analytical solution for the decrease in mean elevation over the bump is given by Longuet-Higgins (1967):

$$\bar{\eta}_{ana} = \frac{k_0 E_0}{\sinh(2k_0 h_0)} - \frac{kE}{\sinh(2kh)} \tag{28}$$

where k is the wavenumber, h is the water depth, E is the variance of the surface elevation, and the subscript $_0$ indicates that the value is taken at $x = 0$.

The configuration of our model for this test case consists of a grid length and width of 800 m and 250 m respectively, a spatial resolution of 5 m,

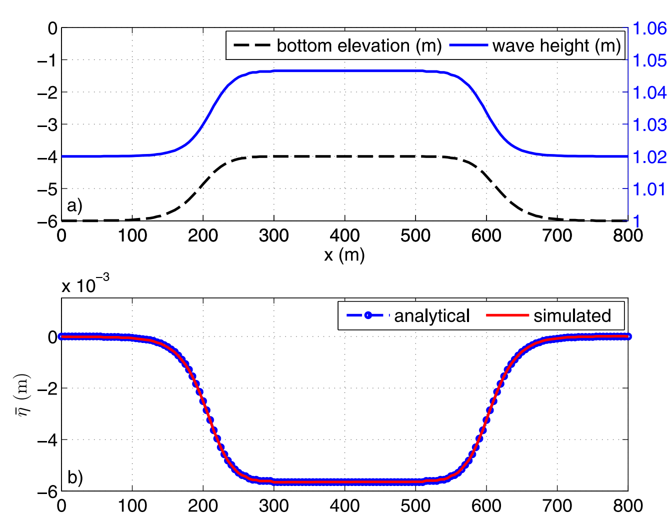

Fig. 13. Adiabatic test case results along the transect $y = 125$ m: (a) bottom elevation and wave height, (b) analytical and simulated mean elevation.

11 vertical sigma-levels, and a time step of 10 s. Fig. 13 shows that the change in surface elevation over the bump is correctly reproduced by the model once the steady state is reached, this change being simply due to the change in wave-induced mean pressure *J* in the framework of the vortex-force formalism.

References

Aagaard, T., Greenwood, B., Hughes, M., 2013. Sediment transport on dissipative, intermediate and reflective beaches. Earth-Sci. Rev. 124, 32–50.
Andrews, D.G., McIntyre, M., 1978. An exact theory of nonlinear waves on a lagrangian-mean flow. J. Fluid Mech. 89 (4), 609–646.
Apotsos, A., Raubenheimer, B., Elgar, S., Guza, R., 2008. Testing and calibrating parametric wave transformation models on natural beaches. Coast. Eng. 55 (3), 224–235.
Apotsos, A., Raubenheimer, B., Elgar, S., Guza, R., Smith, J.A., 2007. Effects of wave rollers and bottom stress on wave setup. J. Geophys. Res. Oceans 112 (C2) Article number C02003.
Ardhuin, F., Jenkins, A.D., Belibassakis, K.A., 2008b. Comments on the three-dimensional current and surface wave equations. J. Phys. Oceanogr. 38 (6), 1340–1350.
Ardhuin, F., Rascle, N., Belibassakis, K.A., 2008a. Explicit wave-averaged primitive equations using a generalized lagrangian mean. Ocean Model. 20 (1), 35–60.
Barthelemy, E., 2017. Rip currents vorticity scaling. Proceedings of the 8th International Conference on Coastal Dynamics. pp. 399–408.
Bennis, A.-C., Ardhuin, F., Dumas, F., 2011. On the coupling of wave and three-dimensional circulation models: choice of theoretical framework, practical implementation and adiabatic tests. Ocean Model. 40 (3), 260–272.
Bennis, A.-C., Dumas, F., Ardhuin, F., Blanke, B., 2014. Mixing parameterization: Impacts on rip currents and wave set-up. Ocean Eng. 84, 213–227.
Bertin, X., Bruneau, N., Breilh, J.-F., Fortunato, A.B., Karpytchev, M., 2012. Importance of wave age and resonance in storm surges: the case xynthia, bay of biscay. Ocean Model. 42, 16–30.
Bertin, X., Castelle, B., Anfuso, G., Ferreira, Ó., 2008. Improvement of sand activation depth prediction under conditions of oblique wave breaking. Geo-Marine Lett. 28 (2), 65–75.
Bertin, X., Castelle, B., Chaumillon, E., Butel, R., Quique, R., 2008. Longshore transport estimation and inter-annual variability at a high-energy dissipative beach: St. Trojan beach, Sw Oléron Island, France. Cont. Shelf Res. 28 (10), 1316–1332.
Bertin, X., Chaumillon, E., Sottolichio, A., Pedreros, R., 2005. Tidal inlet response to sediment infilling of the associated bay and possible implications of human activities: the Marennes-Oléron bay and the Maumusson Inlet, France. Cont. Shelf Res. 25 (9), 1115–1131.
Bertin, X., Li, K., Roland, A., Bidlot, J.-R., 2015. The contribution of short-waves in storm surges: two case studies in the bay of biscay. Cont. Shelf Res. 96, 1–15.
Bertin, X., Olabarrieta, M., MacCall, R., 2017. Hydrodnamics under storm conditions, in Coastal Storms: Processes and Impacts. John Wiley and Son.
Bertin, X., Oliveira, A., Fortunato, A.B., 2009. Simulating morphodynamics with unstructured grids: description and validation of a modeling system for coastal applications. Ocean Model. 28 (1-3), 75–87. http://dx.doi.org/10.1016/j.ocemod.2008.11.001.
Bertin, X., Prouteau, E., Letetrel, C., 2013. A significant increase in wave height in the North Atlantic Ocean over the 20th century. Global Planet. Change 106, 77–83. Cited By 9
Bishop, C., Donelan, M., 1987. Measuring waves with pressure transducers. Coast. Eng. 11 (4), 309–328. http://dx.doi.org/10.1016/0378-3839(87)90031-7.
Bruneau, N., Bonneton, P., Castelle, B., Pedreros, R., 2011. Modeling rip current circulations and vorticity in a high-energy mesotidal-macrotidal environment. J. Geophys. Res. Oceans 116 (7) Article number C07026.
Cacina, N., 1989. Test and evaluation of surf forecasting model. Technical Report. Naval Postgraduate School Monterey CA.
Dally, W.R., Osiecki, D.A., 1995. The role of rollers in surf zone currents. Coastal Engineering 1994. pp. 1895–1905.
Delpey, M., Ardhuin, F., Otheguy, P., Jouon, A., 2014. Effects of waves on coastal water dispersion in a small estuarine bay. J. Geophys. Res. Oceans 119 (1), 70–86.
Dodet, G., Bertin, X., Bruneau, N., Fortunato, A.B., Nahon, A., Roland, A., 2013. Wave-current interactions in a wave-dominated tidal inlet. J. Geophys. Res. Oceans 118 (3), 1587–1605.
Eldeberky, Y., Battjes, J.A., 1996. Spectral modeling of wave breaking: application to Boussinesq equations. J. Geophys. Res. Oceans 101 (C1), 1253–1264.
Feddersen, F., 2012. Scaling surf zone turbulence. Geophys. Res. Lett. 39 (18).
Fortunato, A.B., Freire, P., Bertin, X., Rodrigues, M., Ferreira, J., Liberato, M.L., 2017. A numerical study of the February 15, 1941 storm in the Tagus estuary. Cont. Shelf Res. 144, 50–64.
Garcez-Faria, A., Thornton, E., Lippmann, T., Stanton, T., 2000. Undertow over a barred beach. J. Geophys. Res. Oceans 105 (C7), 16999–17010.
Grant, W.D., Madsen, O.S., 1979. Combined wave and current interaction with a rough bottom. J. Geophys. Res. Oceans 84 (C4), 1797–1808.
Hamm, L., Peronnard, C., 1997. Wave parameters in the nearshore: a clarification. Coast. Eng. 32 (2-3), 119–135.
Kennedy, A., Westerink, J., Smith, J., Hope, M., Hartman, M., Taflanidis, A., Tanaka, S., Westerink, H., Cheung, K., Smith, T., Hamann, M., ad Minamide, M., Ota, A., Dawson, C., 2012. Tropical cyclone inundation potential on the hawaiian islands of Oahu and Kauai. Ocean Model. 52-53, 54–68.
Komen, G.J., Cavaleri, L., Donelan, M., Hasselmann, K., Hasselmann, S., Janssen, P.A.E.M., 1996. Dynamics and Modelling of Ocean Waves. Cambridge University Press.
Kumar, N., Voulgaris, G., Warner, J.C., Olabarrieta, M., 2012. Implementation of the vortex force formalism in the coupled ocean-atmosphere-wave-sediment transport (coawst) modeling system for inner shelf and surf zone applications. Ocean Model. 47, 65–95.
Longuet-Higgins, M.S., 1967. On the wave-induced difference in mean sea level between the two sides of a submerged breakwater. J. Mar. Res. 25, 148–153.
Longuet-Higgins, M.S., Stewart, R., 1964. Radiation stresses in water waves; a physical discussion, with applications. Deep Sea Research and Oceanographic Abstracts. 11. Elsevier, pp. 529–562.
Malhadas, M.S., Leitão, P.C., Silva, A., Neves, R., 2009. Effect of coastal waves on sea level in Óbidos Lagoon, Portugal. Cont. Shelf Res. 29 (9), 1240–1250.
Mellor, G., 2003. The three-dimensional current and surface wave equations. J. Phys. Oceanogr. 33 (9), 1978–1989.
Mellor, G., 2016. On theories dealing with the interaction of surface waves and ocean circulation. J. Geophys. Res. Oceans 121 (7), 4474–4486.
Michallet, H., Cienfuegos, R., Barthélemy, E., Grasso, F., 2011. Kinematics of waves propagating and breaking on a barred beach. Eur. J. Mech. B/Fluids 30 (6), 624–634.
Moghimi, S., Klingbeil, K., Gräwe, U., Burchard, H., 2013. A direct comparison of a depth-dependent radiation stress formulation and a vortex force formulation within a three-dimensional coastal ocean model. Ocean Model. 70, 132–144.
Moghimi, S., Thomson, J., Özkan-Haller, T., Umlauf, L., Zippel, S., 2016. On the modeling of wave-enhanced turbulence nearshore. Ocean Model. 103, 118–132.
Nicolae-Lerma, A., Bulteau, T., Lecacheux, S., Idier, D., 2015. Spatial variability of extreme wave height along the atlantic and channel french coast. Ocean Eng. 97 (-), 175–185.
Nicolae-Lerma, A., Pedreros, R., Robinet, A., Sénéchal, N., 2017. Simulating wave setup and runup during storm conditions on a complex barred beach. Coast. Eng. 123, 29–41.
Olabarrieta, M., Warner, J., Kumar, N., 2011. Wave-current interaction in Willapa Bay. J. Geophys. Res. Oceans 116 (12).
Raubenheimer, B., Guza, R., Elgar, S., 1996. Wave transformation across the inner surf zone. J. Geophys. Res. Oceans 101 (C11), 25589–25597.
Raubenheimer, B., Guza, R., Elgar, S., 2001. Field observations of wave-driven setdown and setup. J. Geophys. Res. Oceans 106 (C3), 4629–4638.
Roelvink, J., Stive, M., 1989. Bar-generating cross-shore flow mechanisms on a beach. J. Geophys. Res. 94 (C4), 4785–4800.
Roland, A., Zhang, Y.J., Wang, H.V., Meng, Y., Teng, Y.-C., Maderich, V., Brovchenko, I., Dutour-Sikiric, M., Zanke, U., 2012. A fully coupled 3D wave-current interaction model on unstructured grids. J. Geophys. Res. 117 Article number C00J33.
Saied, U., Tsanis, I., 2008. A coastal area morphodynamics model. Environ. Model. Softw. 23 (1), 35–49.
Sallenger, A.H., Holman, R.A., 1985. Wave energy saturation on a natural beach of variable slope. J. Geophys. Res. Oceans 90 (C6), 11939–11944.
Salmon, J., Holthuijsen, L., Zijlema, M., van Vledder, G.P., Pietrzak, J., 2015. Scaling depth-induced wave-breaking in two-dimensional spectral wave models. Ocean Model. 87, 30–47.
Saville, T., 1961. Experimental determination of wave set-up. Proceedings of the Second Technical Conference on Hurricanes, US Dept. of Commerce, National Hurricane Res. Proj., 1961. pp. 242–252.
Svendsen, I.A., 1984. Wave heights and set-up in a surf zone. Coast. Eng. 8 (4), 303–329.
Terray, E., Donelan, M., Agrawal, Y., Drennan, W., Kahma, K., Williams, A.J., Hwang, P., Kitaigorodskii, S., 1996. Estimates of kinetic energy dissipation under breaking waves. J. Phys. Oceanogr. 26 (5), 792–807.
The SWAN Team, 2014The SWAN Team. SWAN Scientific and Technical Documentation. Delft University of Technology.
Thornton, E., Humiston, R., Birkemeier, W., 1996. Bar/trough generation on a natural beach. J. Geophys. Res. Oceans 101 (C5), 12097–12110.
Thornton, E.B., Guza, R., 1983. Transformation of wave height distribution. J. Geophys. Res. Oceans 88 (C10), 5925–5938.
Uchiyama, Y., McWilliams, J.C., Shchepetkin, A.F., 2010. Wave–current interaction in an oceanic circulation model with a vortex-force formalism: application to the surf zone. Ocean Model. 34 (1), 16–35.
Umlauf, L., Burchard, H., 2003. A generic length-scale equation for geophysical turbulence models. J. Marine Res. 61 (2), 235–265.
Zhang, Y., Baptista, A.M., 2008. SELFE: a semi-implicit Eulerian–Lagrangian finite-element model for cross-scale ocean circulation. Ocean Model. 21 (3-4), 71–96.
Zhang, Y.J., Ye, F., Stanev, E.V., Grashorn, S., 2016. Seamless cross-scale modeling with schism. Ocean Model. 102, 64–81.